Zeroth and first-order homogenized approximations to nonlinear diffusion through block inclusions by an analytical approach

R.F. Sviercoski [a,b,*], P. Popov [b], B.J. Travis [a]

[a] Los Alamos National Laboratory, Mail Stop F665, Los Alamos, NM 87545, United States
[b] Department of Mathematics and Institute for Scientific Computation, Texas A&M University, College Station, TX 77840, United States

ABSTRACT

Approximate solutions to nonlinear diffusion systems are useful for many applications in computational science. When the heterogeneous nonlinear diffusion coefficient has high contrast values, an average solution given by upscaling the diffusion coefficient provides the average behavior of the fine-scale solution, which sometimes is infeasible to compute. This is also related to a problem that occurs during numerical simulations when it is necessary to coarsen meshes and an upscale coefficient is needed in order to build the data from the fine mesh to the coarse mesh. In this paper, we present a portable and computationally attractive procedure for obtaining not only the upscaled coefficient and the zeroth-order approximation of nonlinear diffusion systems, but also the first-order approximation which captures fine-scale features of the solution. These are possible by considering a correction to an approximate solution to the well known periodic cell-problem, obtained by a two-scale asymptotic expansion of the respective nonlinear diffusion equation. The correction allows one to obtain analytically the upscale diffusion coefficient, when the heterogeneous coefficient is periodic and rapidly oscillating describing inclusions in a main matrix. The approximate solutions provide a set of analytical basis functions used to construct the first-order approximation and also an estimate for the upper bound error implied in using the upscaled approximations. We demonstrate agreement with theoretical and published numerical results for the upscale coefficient, when heterogeneous coefficients are described by step-functions, as well as convergence properties of the approximations, corroborating with classical results from homogenization theory. Even though the results can be generalized, the emphasis is for conductivity functions of the form $\mathbf{K}(x, u(x)) = \mathbf{K}_s(x)k_r(u(x))$, widely used for simulating flows in reservoirs.

Published by Elsevier B.V.

1. Introduction

Many important problems in science and engineering fields such as material science, earth and environmental sciences, petroleum and chemical engineering, involve solving a nonlinear diffusion equation with highly oscillating heterogeneous coefficients. One example occurs in modeling flow and transport in natural porous media since geological formations are characterized by heterogeneity at multiple length scales. These problems are often difficult to solve by direct numerical simulation due to their expensive computational requirements. Because of that, upscaling or homogenization techniques are often employed in order to obtain macroscopic approximations of the flow behavior and to minimize computational efforts.

Existing upscaling techniques for flow through porous media are reviewed in Hornung [14]. Our multiscale approximation is

based on the two-scale method presented in Bensoussan et al. [4], Sanchez-Palencia [24], Jikov et al. [17], and Bourgeat [6] among many others.

The problem in obtaining multiscale approximations starts with computing the zeroth-order approximation or the averaged macroscopic flow behavior. If each grid block represents one type of heterogeneity, such as the example presented in [2], the computational cost involved in obtaining the effective coefficient may exceed the cost of solving the fine-scale problem. Moreover, it often requires special code design, which may also add to coding time and reduce performance. Because of such constraints, obtaining the macroscopic solution of a given nonlinear system, feasible for field scale simulations, is still a challenging problem. Intensifying further the challenge is the addition of small scales features into the solution, given by the first-order approximation. Therefore it is desirable to develop a portable algorithm, applicable to existing codes, that not only captures the macroscopic behavior, but also adds fine-scale features into the solution of a generalized nonlinear solution.

The goals of this paper are two-fold. First, an analytical closed form approximation of the effective macroscopic diffusion

* Corresponding author. Address: Department of Mathematics and Institute for Scientific Computation, Texas A&M University, College Station, TX 77840, United States. Tel.: +1 505 665 2871.
E-mail addresses: rsviercoski@math.tamu.edu, rsvier@lanl.gov (R.F. Sviercoski).

coefficient is proposed for nonlinear diffusion equations that are relevant to flow in porous media. The approach also leads to an analytical approximation to the cell solutions, used to construct a first-order approximation to the fine-scale nonlinear solution. Secondly, we demonstrate, by numerical means, convergence properties for both the zeroth and first-order approximations to the fine-scale solutions, that corroborates theoretical convergence results from the classical literature.

The results are based on an analytical approximation to the solutions of the canonical cell problems for the diffusion equation (c.f. e.g. [4,7,17,24]). The approximation was proposed in Sviercoski et al. [25] for linear diffusion equation with step function coefficients including periodic fine-scale geometries, leading to an effective coefficient in agreement with the lower bound of the generalized Voigt–Reiss' inequality [17, Eq. 1.74]. The advantage of the current approach is that in addition to the macroscopic coefficient it also provides an approximation to the solution of the canonical cell-problems and thus can be used to construct first-order correctors. For the class of nonlinear problems under consideration, the analytically upscaled coefficient is computed only once and then used in the solution to the nonlinear diffusion equation, implying significant savings in computational effort, compared to general nonlinear solver formulations. Moreover, an indicator for an upper bound estimate of the error between the exact fine-scale solution and the approximations is proposed. The results presented are an extension of the linear case from Sviercoski et al. [26].

Among many numerical multiscale approaches applicable to the nonlinear case, a certainly non exhaustive list includes the variational approaches [3,16], adaptive modeling algorithms [20], the domain decomposition [22], the two-grid technique [30] and the equivalent block permeability by numerical means [1,2,9]. Our result can be considered as an analytical version of the nonlinear multiscale finite element method (MsFEM) of Efendiev et al. [10–13]. The MsFEM provides a way of obtaining a numerical first-order solution by constructing a finite element basis function from a numerical solution of the cell-problem built into the coarse scale through the global stiffness matrix. Here, the differences are: the effective coefficient is explicitly computed by analytical means, and an analytical approximation to the basis function is applied, which is the major advantage here since in practice, a large amount of overhead time comes from constructing basis functions [15]. Moreover the approximation for the basis function is obtained for the whole domain; it is a local–global approach that avoids resonance errors reported in Hou et al. [15]. Another advantage compared with other multiscale numerical procedures, is the ability to get an estimate for the upper bound error (UBE) implied in using the approximations. Error estimates are very important in multiscale modeling, and the approach presented here can be further exploited in the context of adaptive modeling algorithms, such as Oden et al. [20].

The nonlinear diffusion system, considered in this paper, assumes that the conductivity function is of the form $\mathbf{K}(x, u(x)) = \mathbf{K}_s(x)k_r(u(x))$, and $k_r(u(x))$ is the same form throughout the domain in consideration. This form of nonlinearity is commonly used in Petroleum Engineering and Soil Sciences [29], where Darcy's law describes the velocity of a wetting front. Moreover, the system is such that the capillary forces are dominant, meaning that the flow behavior has a finite Peclet number. Theoretical results for upscaling such systems are presented in Bourgeat [6], and literature herein. The fact that we present results for periodic media might be a limitation of the procedure, however it is a necessary step towards generalized cases. Because the first-order approximation is proposed, there is no constraint regarding the separation of scales, which is the case when only the zeroth-order is considered.

Besides flow in porous media, the method applies to other areas and aspects of computational sciences, such as effective diffusivity

when averaged concentration is considered and, elastic modulus, when averaged displacement needs to be calculated [24]. The results have also the potential to be applied to multilevel iterative solvers [21].

The paper is organized as follows: In Section 2, we briefly review homogenization theory and the main results that will be used in the paper. In Section 3, we review recent analytical results that allow one to obtain an upscaled coefficient and a first-order approximation. In Section 4, we present numerical results by first comparing the upscaled value with analytical and numerical results from the literature and second, demonstrating numerically convergence properties, by using different types of boundary conditions and nonlinearity relationships. Moreover, one of the examples includes gravity forcing. The oscillating coefficients are, without loss of generality, described by square and circular inclusions (in 2-D) in a primary matrix, with contrast ratios being 1000:1, 1:100, 1e−07:1e−02.

2. Diffusion in nonlinear periodic media

In this section, we consider the nonlinear diffusion boundary value problem (BVP) in ε-periodic heterogeneous media:

$$-\nabla \cdot (\mathbf{K}^\varepsilon(x, u^\varepsilon)\nabla u^\varepsilon(x)) = f(x) \quad x \in \Omega, \tag{1}$$

$$u^\varepsilon(x) = g(x) \quad x \in \partial\Omega, \tag{2}$$

where $u^\varepsilon(x) = u(\varepsilon^{-1}x)$ and $\varepsilon = \frac{l}{L}$ is the scale parameter defined as the ratio between the characteristic length of the small structure, l, and the macroscopic length scale L. The conductivity function is the diagonal matrix:

$$\mathbf{K}^\varepsilon(x, u^\varepsilon) = K^\varepsilon(x, u^\varepsilon)\mathbf{I} = K_s^\varepsilon(x)k_r(u^\varepsilon(x))\mathbf{I}. \tag{3}$$

where $\mathbf{I}$ is the identity matrix and $K_s^\varepsilon(\cdot)$ is the known saturated hydraulic conductivity or absolute permeability which quantifies the ability of the medium to transmit any single-phase fluid and, the superscript ε denotes that this coefficient is the periodic part of $\mathbf{K}^\varepsilon$. The scalar function $k_r(\cdot)$ is the relative permeability, which depends on the pressure (through saturation) to account for the wetting phase and is usually obtained by laboratory experiments, having parameters reflecting the soil type [29]. The fluid velocity is related to the pressure field through Darcy's law:

$$\mathbf{q}^\varepsilon(x) = -\frac{1}{\mu}\mathbf{K}^\varepsilon(x, u^\varepsilon)\nabla u^\varepsilon(x), \tag{4}$$

where μ is the fluid viscosity.

Next the classical upscaling of the above equation is described. We introduce the fast variable $y = \varepsilon^{-1}x = (y_1, y_2, \ldots y_n) \in Y = [0, 1]^n$, and the formal two-scale asymptotic expansion of (1) [4,24,28], is considered:

$$u^\varepsilon(x) = u^0(x, y) + \varepsilon u^1(x, y) + \varepsilon^2 u^2(x, y) + \ldots, \tag{5}$$

where each term $u^i(x, y)$ is periodic in y. By substituting (5) into (1), and identifying powers of the small parameter ε we obtain the homogenized system as well as the canonical cell problems.

The formal derivation is not readily available in the literature for nonlinearities of the type (3), and for the sake of clarity, it is given in Appendix A. Here we summarize the main results. The zeroth-order u^0 is found to depend on x only and satisfies the macroscopic equation (c.f. Eq. (46) Appendix A):

$$-\nabla \cdot (\mathbf{K}^0(u^0(x))\nabla u^0(x)) = f(x) \quad x \in \Omega,$$

$$u^0(x) = g(x) \quad x \in \partial\Omega, \tag{6}$$

where the upscaled Darcy's velocity is given by:

$$\mathbf{q}^0(x) = -\frac{1}{\mu}\mathbf{K}^0(u^0(x))\nabla u^0(x). \tag{7}$$

The upscaled coefficient $\mathbf{K}^0$ satisfies (c.f. Eq. (48)):

$$K_{ij}^0(u^0(x)) = k_r(u^0(x)) \int_Y K_s(y) \left(\delta_{ij} + \frac{\partial w^i}{\partial y_j} \right) dy, \tag{8}$$

where δ_{ij} is the *Kronecker delta* and the scalar fields $w^i(y)$, $i = 1, \ldots, n$ are the y-periodic solutions to the n cell-problems:

$$\nabla_y \cdot (\mathbf{K}^\varepsilon(y, u^0(x)) \nabla_y w^i(y)) = -\nabla_y \cdot (\mathbf{K}^\varepsilon(y, u^0(x)) e_i) \quad y \in Y, \tag{9}$$

where e_i, $i = 1, \ldots, n$ is the ith coordinate direction. Because of the multiplicative form of conductivity (3), the last equation simplifies to give

$$\nabla_y \cdot (K_s(y) \nabla_y w^i(y)) = -\nabla_y \cdot (K_s(y) e_i) \quad y \in Y, \tag{10}$$

and the form (8) follows. Thus, the cell problem involves only the absolute permeability K_s and is of the same type as the canonical cell problems for the linear diffusion equation. It should be noted that if the multiplicative decomposition (3) did not hold one would instead have cell problems that are coupled to the coarse scale Eq. (6). The theoretical justification for (6)–(10), based on a fine-scale coefficient of the type (3) can be found in Bourgeat [6] who demonstrated that in the limit $\varepsilon \to 0$:

$$u^\varepsilon(x) \to u^0(x) \text{ in } L^2(\Omega), \tag{11}$$

$$\mathbf{K}^\varepsilon(u^\varepsilon(x)) \nabla u^\varepsilon(x) \rightharpoonup \mathbf{K}^0(u^0(x)) \nabla u^0(x) \text{ in } (L^2(\Omega))^n. \tag{12}$$

Because we emphasize numerical convergence properties, we constrain ourselves to the Hilbert Space $L^p(\Omega)$ for $p = 2$, but analogous results follow for $1 \leqslant p < \infty$. We also recall that if a function and its derivative belongs to $L^2(\Omega)$, then it belongs to the subspace $H^1(\Omega)$. Functions in $H^1(\Omega)$ have a higher degree of smoothness compared to the ones belonging only to $L^2(\Omega)$. An illustration of the difference between functions on each of these spaces is shown in Fig. 1 ahead. Now, strong convergence is achieved for the solution itself but only weak convergence is proven for the flux. A reminder of the difference between these two types of convergence can be given by considering the function $f^\varepsilon(x) = \sin(\varepsilon^{-1}x)$, which converges weakly in L^2 to $f^0(x) = 0$ but the convergence is not in the strong sense. This will be also revealed in the examples on Section 4.2.

The limiting or upscale solution, $u^0(x)$, provides a smooth approximation to $u^\varepsilon(x)$ (see Fig. 6). In order to obtain an approximation that captures fine-scale details of $u^\varepsilon(x)$, one retains the first two terms in the expansion (5), denoted by the subscript "1" to not confuse with the first-order term of the expansion, as:

$$u_1^\varepsilon = u^0(x) + \varepsilon u^1(x, y), \tag{13}$$

where $\varepsilon u^1(x, y)$ is defined as:

$$\varepsilon u^1(x, y) = \sum_{i=1}^n w^i(y, u^0(x)) \frac{\partial u^0(x)}{\partial x_i}. \tag{14}$$

The solutions $w^i(y, u^0(x))$ of Eqs. (9) and (10) contain fine-scale features and are used as basis functions to construct the first-order expansion of $u^\varepsilon(x)$.

The following two-scale expansion for the gradient is known for the linear case (c.f. [7] and literature herein):

$$\begin{aligned} \nabla u^\varepsilon(x) &= \nabla u^0(x) + \varepsilon \nabla u^1(x, y) + \ldots. \\ &= \nabla u^0(x) + \nabla_y u^1(x, y) + \varepsilon \nabla_x u^1(x, y) + \ldots. \\ &= \nabla u^0(x) + \nabla_y \mathbf{w}(y) \nabla u^0(x) + \mathbf{w} \nabla(\nabla u^0(x)) + \ldots \\ &= (\mathbf{I} + \nabla_y \mathbf{w}(y)) \nabla u^0(x) + \varepsilon \mathbf{w} \nabla(\nabla u^0(x)) + \ldots, \end{aligned} \tag{15}$$

where $\mathbf{w} = (w^1, \ldots, w^n)$, $\nabla_y \mathbf{w} = \left(\frac{\partial \mathbf{w}}{\partial y_1}, \ldots, \frac{\partial \mathbf{w}}{\partial y_n} \right)^t$, and $\frac{\partial \mathbf{w}}{\partial y_i} = \left(\frac{\partial w^1}{\partial y_i}, \ldots, \frac{\partial w^n}{\partial y_i} \right)$.

From the last equation, a corrector function to the gradient is defined as the matrix

$$\mathbf{C}(y) = \mathbf{I} + \nabla_y \mathbf{w}(y). \tag{16}$$

Also, from ([7], Th. 8.6) we know that:

$$\|\nabla u^\varepsilon(x) - \mathbf{C}(y) \nabla u^0(x)\|_2 \to 0 \text{ in} (L^2(\Omega))^n. \tag{17}$$

The corrector $\mathbf{C}(y)$ incorporates fine-scale features into $\nabla u^0(x)$, allowing an approximation in the strong sense to $\nabla u^\varepsilon(x)$.

Even though (15)–(17) were developed for the linear case, the result will be applied, in the next section, to the nonlinear case presented in this paper. To get there, we will first present an analytical approximation to the cell problem (10) and a corrector term, derived from $\mathbf{C}(y)$, leading to an approximation to the effective coefficient (8) and (6). Based also on this corrector, approximations will follow for the basis function, for the first-order term $u^1(x, y)$ (14), and for the gradient and flux.

3. Analytical approximations

The analytical result presented in this section is based upon a closed form approximation to the solution of the cell problem (10). Let us first define the function

$$G_i(y_1, \ldots, y_i, \ldots, y_n, u^0) = \int_0^{y_i} \frac{d\tau}{K(y_1, \ldots, y_{i-1}, \tau, y_{i+1}, \ldots, y_n, u^0)},$$

and note that the harmonic average, H_i, in the ith coordinate direction is:

$$H_i(y_1, \ldots, y_{i-1}, y_{i+1}, \ldots, y_n, u^0) = \left(\int_0^1 \frac{dy_i}{K(y_1, \ldots, y_n, u^0)} \right)^{-1}.$$

Observe, that $H_i(y_1, \ldots, y_{i-1}, y_{i+1}, \ldots, y_n, u^0) = G_i(y_1, \ldots, 1, \ldots, y_n, u^0)^{-1}$. Now, let us define the general approximation $\tilde{w}^i$ to the solution of the ith cell problem (10) as:

$$\tilde{w}^i(y) = \frac{G_i(y_1, \ldots, y_i, \ldots, y_n, u^0)}{G_i(y_1, \ldots, 1, \ldots, y_n, u^0)} - y_i = \int_0^{y_i} \frac{dy_i}{K_s(y)} \left(\int_0^1 \frac{dy_i}{K_s(y)} \right)^{-1} - y_i. \tag{18}$$

This construction follows the same approach as [25], where a linear diffusion equation with heterogeneous coefficients is considered. Note that, while in the current work G_i and H_i depend on u^0, thanks to (3) this dependence cancels out and $\tilde{w}_i$ is a function of y only. This is consistent with Eq. (9) reducing to the equivalent (10).

The function defined in (18) is an n-dimensional approximation to the solutions of the cell problems (10). In some special cases, such as one-dimensional media, layered media, or media with spatially separable coefficient K, this approximation reduces to the respective exact solution, as described below:

(R1) – In 1-D, one can directly verify that $\tilde{w}^1(y)$ solves (10). Furthermore, by substituting it into (8) the well known harmonic average H_1 is obtained for the upscaled coefficient K_s^0 (c.f. e.g. [14]).
(R2) – When $K_s(y)$ describes a layered media, then the substitution of (18) into (8), leads to the known diagonal tensor (c.f. e.g. [14]) with the arithmetic average of $K_s(y)$ as the components in directions parallel to the layers and the harmonic average of $K_s(y)$ in the direction perpendicular to the layers. Indeed, suppose without loss of generality, that the media has layers perpendicular to the y_1 direction, then the harmonic average H_1 is a constant and substituting (18) into (8) yields H_1 as the upscaled component in that direction. For $i \neq 1$, $\tilde{w}^i(y) = 0$ and (8) yields the arithmetic average of $K_s(y)$ as the upscaled component in those directions.
(R3) – If $K_s(y) = \Pi_i k_i(y_i)$, that is, a spatially separable coefficient, then (18) will give the effective coefficient as the diagonal
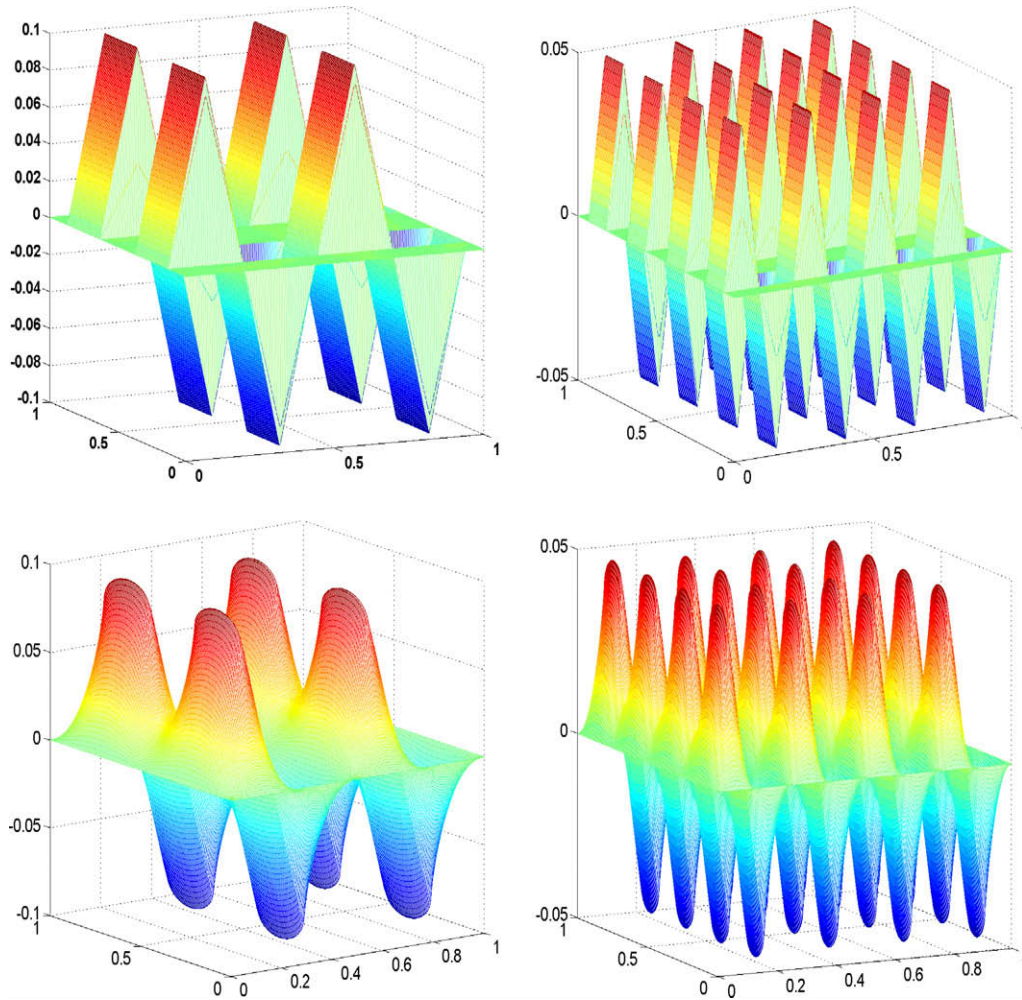
Fig. 1. Top: Analytical approximations $\bar{w}^i(\varepsilon^{-1}x) \in L^2(\Omega)$ for $\varepsilon = 0.25$ and $\varepsilon = 0.125$, meaning 4 and 16 square inclusions, respectively, and inclusion ratio 10:1. **Bottom** their numerical counterpart, $w^i(\varepsilon^{-1}x) \in H^1(\Omega)$. Observe that their main heterogeneity features, such as number of critical points, maximum and minimum values, and the zero mean, are preserved. The main difference is the smoothness.

matrix with entries given as the arithmetic average of the harmonic average ([17, Eq. 1.28]).

In Sviercoski et al. [25], it has been shown that when $K_s(y)$ is given as a step function coefficient, then $\tilde{w}^i(y) \in L^2(Y)$ is an approximation to (10). Furthermore, when the coefficient is symmetrically centered in the Y-cell, meaning that $K_s(y)$ is periodic with center of mass being at half of the period and invariant under $\pi/2$ rotation, the results follow:

(**R4**) $\int_Y \bar{w}^i(y)dy = 0$.
(**R5**) $\int_Y K_s(y) \frac{\partial \tilde{w}^i}{\partial y_j} dy = 0$ for $j \neq i$.
(**R6**) $\int_Y \bar{w}^i(y)\bar{w}^j(y)dy = 0$ $i \neq j$.

Even though these results were applied to step function coefficients, here this condition is generalized to any type of coefficient functions such that the heterogeneity is symmetrically centered in the unit cell. (**R4**)–(**R6**) also justify the choice of $\tilde{w}^i(y)$, $i = 1, \ldots, n$ as candidates to the basis functions in (13). Note that $\tilde{w}^i(y)$ can be defined on the whole domain Ω, not only over the cell Y, and because of the periodicity, the same results above apply to Ω. A comparison between $w^i(y) \in H^1(\Omega)$, the solution to (10), and its approximation $\tilde{w}^i(y) \in L^2(\Omega)$ is illustrated in Fig. 1, for the particular case when the inclusions have a square shape. Note that they

agree in most of the features, including number of critical points, maximum, minimum and zero mean values. They differ in smoothness.

The substitution of (18) into the integrand of (8) and (**R5**) leads to:

$$\widetilde{K}(u^0(x)) = diag\left(\int_Y H_1(y)dY, \ldots, \int_Y H_n(y)dY \right) k_r(u^0)$$
$$= \widetilde{K}_s k_r(u^0) \tag{19}$$

and the following result holds:

(**R7**) $\widetilde{K}_s$ is the lower bound of the generalized Voigt–Reiss' inequality (Jikov et al. [17, Eq. 1.74]):

$$\widetilde{K}_s \leqslant K_s^0 \leqslant K_s^u, \tag{20}$$

where the upper bound is defined as $K_{s_{ii}}^u = \left(\int_Y \frac{dy_j}{\int_Y K_s(y)dy_i} \right)^{-1}$, with $j \neq i$.

This shows that $\widetilde{K}_s$ is not new in the literature. Inequality (20) is a more accurate two-sided estimate for isotropic effective coefficient than the classical Voigt–Reiss' inequality (also known as Wiener bounds [23]), stating that K_s^0 lies between the harmonic and arithmetic averages of $K_s(y)$. In [17] they obtained the lower and upper bound by variational principle. What is new is that $\tilde{w}^i(y)$ is

an explicit *n*-dimensional minimizer of the energy functional considered by [17]. The advantage of such findings is that one can use these approximations to obtain a corrector and therefore a more accurate approximation to K_s^0, moreover they also provide a way of obtaining an approximation to the first-order (13), as it will be shown next.

3.1. An analytical approximation to K^0

It can be verified that $\widetilde{K}_s = K_s^0$ for the classical cases discussed in (**R1**)–(**R3**). For all the other cases, $\widetilde{K}_s$ is, at least, a lower bound, and therefore a correction is needed. We first recall that in [7] and literature herein, the corrector function $\mathbf{C}(y)$ (16) is also used as a multiplicative function for correcting the effective coefficient K^0, as $\mathbf{C}(y)K^0$. We use similar idea to construct a constant corrector to the lower bound $\widetilde{K}_s$. In this sense, we first define our corrector function, using $\tilde{w}^i(y)$ from (18) instead of $w^i(y)$ into the definition of the matrix corrector $\mathbf{C}(y)$ from (16), to obtain the diagonal corrector functions:

$$\widetilde{C}_{ii}(y) = 1 + \frac{\partial \tilde{w}^i}{\partial y_i} = \frac{1}{K_s(y)}\left(\int_0^1 \frac{dy_i}{K_s(y)}\right)^{-1} = \frac{H_i}{K_s(y)}. \quad (21)$$

Each $\widetilde{C}_{ii}(y)$ is a dimensionless function having the property $\int_Y \widetilde{C}_{ii}(y)dy = 1$. By computing the L^2-norm of these functions, a corrector to $\widetilde{K}_s$ can be obtained. The product:

$$(\widetilde{K}_s^0)_{ii} = \|\widetilde{C}_{ii}(y)\|_2(\widetilde{K}_s)_{ii} = \widetilde{C}_i(\widetilde{K}_s)_{ii} \quad (22)$$

corresponds to a correction to the *i*th diagonal of $\widetilde{\mathbf{K}}_s$, and a more accurate approximation to (8) is obtained as:

$$K^0(u^0(x)) \approx \widetilde{\mathbf{C}}\widetilde{K}_s k_r(u^0(x))\mathbf{I} = \widetilde{K}_s^0 k_r(u^0(x))\mathbf{I} = \widetilde{K}^0. \quad (23)$$

where $\widetilde{\mathbf{C}} = diag(\widetilde{C}_1, \ldots, \widetilde{C}_n)$ and $\widetilde{C}_i = \|\widetilde{C}_{ii}(y)\|_2$. The L^2-norm is reasonable to consider as it is a constant that does not depend on ε, which is greater than or equal to 1. It also relates to the root mean square of the error implied by using $\tilde{w}^i$, instead of w^i, in the definition of K_s^0. Indeed, if an error function $r_i(y) > 0$ is added to the *i*th diagonal entry of $\widetilde{K}_s$ to account for the approximation to K_s^0, then by requiring this component to be positive, $F_i(y) = K_s(y)\left(1 + \frac{\partial \tilde{w}^i}{\partial y_i} + r_i(y)\right) > 0$ implies that $r_i(y) > -\widetilde{C}_{ii}(y)$, which is always satisfied. Note also that $\|r_i(y) + \widetilde{C}_{ii}(y)\|_2 = b$ and $\|r_i(y)\|_2 \leqslant \widetilde{C}_i + b$.

The corrector is also applied to (18) to get an approximation to the basis functions (10), as:

$$\tilde{w}_c^i(y) = \widetilde{C}_i \tilde{w}^i(y). \quad (24)$$

We observe that, by choosing these correctors, the agreements between $\tilde{w}^i(y)$ and $w^i(y)$, pointed out in Fig. 1, and the properties (**R4**) − (**R6**) are still valid when $\tilde{w}_c^i(y)$ is considered. For (**R7**), one can show that $1 \leqslant \widetilde{C}_i \leqslant 2$. These imply that (23) satisfies the generalized Voigt–Reiss' inequality (20) from below, and numerical results, in Section 4, indicate that the upper bound is also satisfied. It will also be shown by numerical means, that the corrector $\widetilde{C}$ plays a crucial role in obtaining an effective coefficient $\widetilde{K}_s^0$ that is in good agreement with numerical and analytical results.

The form of the upscaled coefficient implies that the term $\widetilde{C}_i\widetilde{K}_s$ is computed only once throughout the simulation, even for the transient case, as the dependence on the solution $u^0(x)$ is through the scalar function $k_r(u^0(x))$, that updates at each nonlinear iteration.

In Section 4.2, we use the analytical form (23) to demonstrate that the upscaled approximations (11) and (12) are obtained. For the sake of notation, from now on, we will use $u^0(x)$ to indicate the solution to (6) by using the upscaled coefficient (23).

Moreover, a first-order approximation, similar to (13), is proposed by

$$u^\varepsilon(x) \sim u^0(x) + \varepsilon\tilde{u}^1(x,y) = u^0(x) + \sum_{i=1}^n \widetilde{C}_i\tilde{w}^i(y)\frac{\partial u^0}{\partial x_i} = \tilde{u}_1(x,y). \quad (25)$$

In Section 4.2 ahead, it will be shown numerically that:

$$\|u^\varepsilon(x) - \tilde{u}_1(x,y)\|_2 \to 0 \text{ in } L^2(\Omega). \quad (26)$$

By considering (25), the L^2-norm of $\varepsilon\tilde{u}^1(x,y)$, can be used as an error indicator (UBE), implied by the approximation $u^0(x)$, as

$$\|u^\varepsilon(x) - u^0(x)\|_2 \sim \left\|\sum_{i=1}^n \widetilde{C}_i\tilde{w}^i\frac{\partial u^0(x)}{\partial x_i}\right\|_2 = UBE. \quad (27)$$

The correction to the gradient approximation is carried out from (15) to (16), by replacing $\mathbf{C}(y)$ and $\mathbf{w}$ by $\widetilde{\mathbf{C}}(y)$ and $\widetilde{\mathbf{C}}\bar{\mathbf{w}}$, respectively, to give

$$\nabla u^\varepsilon(x) = \widetilde{\mathbf{C}}(y)\nabla u^0(x) + \varepsilon\widetilde{\mathbf{C}}\tilde{\mathbf{w}}\nabla(\nabla u^0(x)) + \ldots, \quad (28)$$

and an approximation to the first-order of the gradient and flux can be considered. Numerical results ahead show that the error between the gradients

$$\|\nabla u^\varepsilon(x) - \widetilde{\mathbf{C}}(y)\nabla u^0(x)\|_2 \leqslant \alpha_1 \quad (29)$$

and fluxes

$$\|K^\varepsilon(x,u^\varepsilon)\nabla u^\varepsilon(x) - \widetilde{K}^0(u^0(x))(\widetilde{\mathbf{C}}(y)\nabla u^0(x))\|_2 \leqslant \alpha_2, \quad (30)$$

are bounded independently of ε. These imply that convergence for a subsequence is obtained. The boundedness may also be the result of error accumulation in computing the highly oscillating functions. Nevertheless, Figs. 10 and 11 illustrate that $\widetilde{C}_{ii}(y)$ is as highly oscillating as $K_s(y)$ and incorporates heterogeneous features into the homogenized gradient and flux.

Remark – Note that the zeroth-order approximation applies to transient and multiphase cases, as well as to the non-uniform oscillating case, $K_s(x,y)$, when there are several different geological rock facies [6]. However, the only theoretical results, to our knowledge, on convergence properties for the first-order approximation for nonlinear elliptic problems is presented in [4, Eq. 16.27–16.28], where the nonlinearity is not under the divergence operator.

Step function coefficients are widely used in Science and Engineering, particularly in porous media applications. Because of that there are results in the literature for upscaled coefficients computed numerically and analytically. In the next section, we compare these results with our proposed form (23).

4. Numerical results

The goals of this section are two fold. First, we demonstrate agreement between analytical and numerical results and the analytical form (23). Second, we numerically demonstrate convergence properties of the proposed zeroth-order and first-order approximations of (1), with various boundary conditions and different relative permeability forms $k_r(u(x))$.

In all the cases, $K_s(.)$ are periodic functions with the center of mass symmetrically distributed at half of the period. We illustrate the case where they are two-value step functions with ratio $\xi_1:\xi_2$, where ξ_2 is the value in the inclusion. We also confirm that this type of geometry leads to a diagonal upscaled tensor, which is in agreement with (**R5**) above. We present 3 cases; the first one is the well known analytical result regarding the geometric average for checkerboard type of geometry, and the other 2 cases are numerical values, K_n^0, obtained by solving numerically the cell-problem (10) and (8) by various numerical schemes. Since all the upscale tensors are diagonal and isotropic, the values in the following 3 tables are diagonal values, $\widetilde{C}_1 \times \widetilde{K}_s = \widetilde{C}_1\widetilde{K}_s$.

4.1. Comparison of K^0 with theoretical and numerical results

4.1.1. Case 1

The effective coefficient for the checkerboard basic unit cell (Fig. 2) is computed using (23), to demonstrate agreement with the well known result for the geometric average, $K_s^g = \sqrt{\xi_1 \xi_2}$, demonstrated by Keller [18]. The results are shown in Table 1, where our analytic form is shown to provide good to very good agreements.

4.1.2. Case 2

In [1] the effective value K_n^0 was obtained by numerically solving the cell-problem (10) with $Y \subset R^2$ and $K_s(y)$ having ratios 10:1, 100:1, respectively and applied for two-phase nonlinear flow simulation, with $k_r(S(u(x))) = S(u(x))^2(3 - 2S(u(x)))$, S the saturation. Note that here the value for the inclusion is less than the value on the matrix. The geometry for **Test 1**–**Test 3** is illustrated in Fig. 3 (left). The difference between the simulations for **Test 1** and **Test 2** was the viscosity ratio, being 1:1 and 50:1, respectively. Fig. 3 (right) is the geometry used for **Test 4**.

As in Table 1, $\widetilde{\mathbf{C}}$ in Table 2 corrects the lower bound $\widetilde{K}_s$, and inequality (20) is also satisfied.
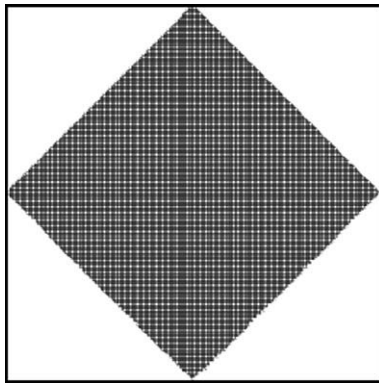

Fig. 2. $K_s(y)$ as the unit cell for the checkerboard structure.

Table 1
Comparison between $\widetilde{K}_s^0$ in column 3 and the geometric average, K_s^g, in column 2. Note that $\widetilde{C}$ indeed corrects $\widetilde{K}_s$. Observe that inequality (20) is also satisfied.

$\xi_1 : \xi_2$	K_s^g (geom. avg.)	$\widetilde{K}_s^0 = \widetilde{C}_1 \times \widetilde{K}_s$	K_s^u (Eq. (20))
5:20	10	**1.0725** × 9.31 = 9.94	10.79
1:10	3.16	**1.1732** × 2.60 = 3.03	3.94
2:8	4	**1.0725** × 3.722 = 3.98	4.34
4:16	8	**1.0725** × 7.4451 = 7.96	8.69
16:4	8	**1.0725** × 7.38 = 7.92	8.64

Table 2
Comparison between $\widetilde{K}_s^0$, column 4, and the numerical values K_n^0, column 3, from [1]. Observe that inequality (20) is also satisfied.

	ratio $\xi_1 : \xi_2$	K_n^0 (from [1])	$\widetilde{K}_s^0 = \widetilde{C}_1 \times \widetilde{K}_s$	K_s^u Eq. (20)	RD $\left(\frac{|K_n^0 - \widetilde{K}_s^0|}{\widetilde{K}_s^0}\right)$ (%)
Test 1	10:1	6.52	**1.093** × 5.91 = 6.459	7.09	1.0
Test 2	10:1	6.52	**1.093** × 5.91 = 6.459	7.09	1.0
Test 3	100:1	59.2	**1.1378** × 51 = 58.03	67	2.0
Test 4	10:1	3.106	**1.0663** × 2.98 = 3.177	3.27	2.0

4.1.3. Case 3

Table 3 shows the comparison between $\widetilde{K}_s^0$ and K_n^0 from [5], where the value was obtained by numerically solving the cell problem for different shapes of inclusions. Three types of inclusions are presented with an area equal to $\frac{1}{4}$, as in Fig. 4, and ratio 1:10. The experiment also illustrates the influence of the shape and surface area of the inclusions in obtaining the effective coefficient. Note that the square and lozenge have the same surface area, which is larger than the circle. Nevertheless, their effective values are different, as well as their lower and upper bounds.

Overall, Tables 1–3 show that our analytical form is accurate for estimating the effective coefficient in agreement with other analytical and numerical results, independently of shape. The common property between the heterogeneous fields was their symmetry. We also observe that the generalized Voigt–Reiss inequality provides more accurate lower and upper bounds than the classical Voigt–Reiss inequality, which can be easily calculated.

Next, we use the analytical form to compute effective values that are placed into the upscaled Eq. (6) to obtain convergence properties of the upscaled solution.

4.2. Numerical convergence results

In this section, we present error analyze illustrating convergence properties between the fine-scale and upscale pressure solutions, by using coefficient functions defined as (31) with ratios 1000:1, 1:100, and 1e−7:1e−2, with square and circular inclusions, without loss of generality.

$K_s^\epsilon(x)$ is the sequence of coefficients that can be formally written as

Table 3
Comparison between $\widetilde{K}_s^0$ (23) and numerical values from [5]. Note how $\widetilde{C}$ corrects the lower bound $\widetilde{K}_s$. Observe that inequality (20) is also satisfied.

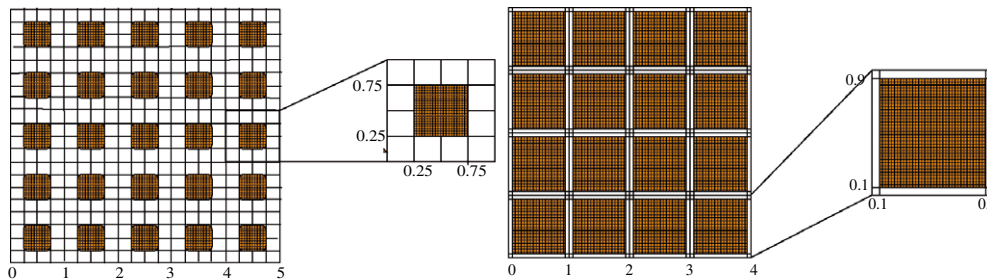| Shape	K_n^0 from [5]	$\widetilde{K}_s^0 = \widetilde{C}_1 \times \widetilde{K}_s$	K_s^u Eq. (20)	RD $\left(\frac{|K_n^0 - K_s^0|}{K_s^0}\right)$ (%)
Square	1.548	**1.0937** × 1.4091 = 1.5411	1.695	0.4
Circle	1.516	**1.08** × 1.403 = 1.5156	1.791	0.02
Lozenge	1.573	**1.069** × 1.417 = 1.5148	1.936	3.7

Fig. 3. (Left) $K_s(y)$ used in Test 1, Test 2 and Test 3; (Right) $K_s(y)$ used in Test 4.
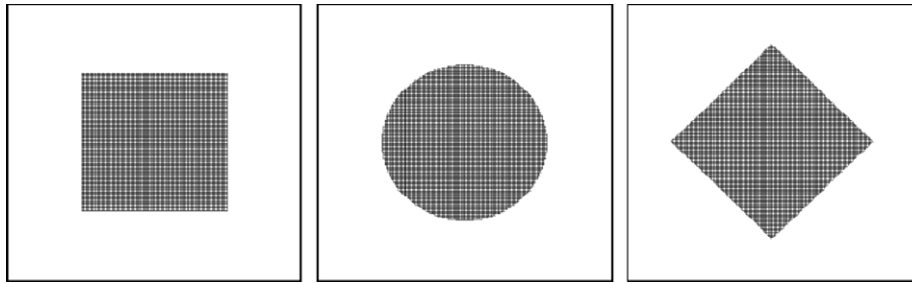
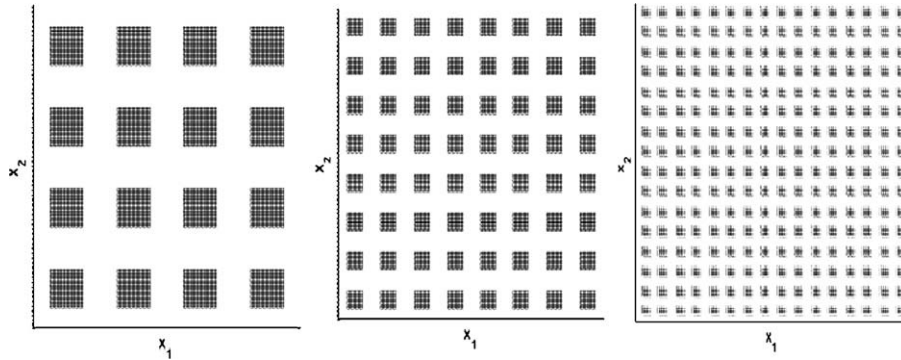**Fig. 4.** Different shapes of inclusions with equal area of $\frac{1}{4}$.

Fig. 5. $K_s^\varepsilon(x)$ for square inclusion and $\varepsilon = (0.5)^3, (0.5)^4, (0.5)^5$, respectively.

$$K_s^\varepsilon(x) = \begin{cases} \xi_1 & \text{if } x \in \Omega^\varepsilon \setminus \Omega_c^\varepsilon, \\ \xi_2 & \text{if } x \in \Omega_c^\varepsilon \end{cases}, \tag{31}$$

with ξ_1 being the value outside the inclusion Ω_c^ε, symmetrically centered in each Ω^ε where $\Omega = \cup_\varepsilon \Omega^\varepsilon$, and $\xi_1 : \xi_2$ is the inclusion ratio. As an example, let Ω_c represent inclusions in (31), occupying $\frac{1}{4}$ of the area of an unit cell, which does not change by varying ε. The sequence $K_s^\varepsilon(x)$ is then constructed by considering $K_s^{0.5}(x)$ having one square or circular inclusion over the unit domain Ω; $K_s^{0.25}(x)$ with four inclusions in the unit domain, until $K_s^{(0.5)^5}(x)$ with 16×16 inclusions. In this process, the degree of heterogeneity of the coefficient is decreasing at the ratio $r = 0.5$, and the initial total volume occupied by the inclusions is preserved, but the total surface area is doubled for each ε. An illustration of $K_s^\varepsilon(x)$-sequence for $\varepsilon = (0.5)^3, (0.5)^4, (0.5)^5$ is given in Fig. 5.

The analysis of the convergence is done by computing the L^2-norm of the error between the heterogeneous or fine-scale solution, $u^\varepsilon(x)$, and the respective approximations obtained on a coarser mesh. The numerical experiments were done by considering $\Omega = [0,1]^2$, without loss of generality.

The general procedure to perform the error analysis, summarized in Tables 4–9, follows:

(**S1**) – Given $K_s(y)$, compute analytically $\widetilde{K}_c^0$ using (23) to obtain $\widetilde{K}^0(u^0) = \widetilde{K}_s^0 k_r(u^0)$, as noted in the Tables.

(**S2**) – For a given BVP, compute numerically the fine-scale solution of (1), the gradients and fluxes on a given mesh.

(**S3**) – From (**S1**), compute the respective $u^0(x)$ by solving (6), $\nabla u^0(x)$ and $K^0(u^0(x)) \cdot \nabla u^0(x)$ on a coarser mesh. The results are then interpolated to the mesh size of the respective fine-scale solution obtained in (**S2**).

(**S4**) – Compute the error between the respective gradients and fluxes, using $\|\nabla f(x)\|_2^2 = \|\partial_{x_1} u(x)\|_2^2 + \|\partial_{x_2} u(x)\|_2^2$;

(**S5**) – Obtain analytically $\tilde{w}^i(y)$ and $\tilde{\mathbf{C}}(y)$ on the same mesh as $u^\varepsilon(x)$.

(**S6**) – Obtain the first-order approximation, using (**S3**) and (**S5**), according to (25).

(**S7**) – Obtain the error indicator (UBE) as in (27);

(**S8**) – Compute the error between the gradients from (29);

(**S9**) – Compute the error between the fluxes from (30);

(**S1**)–(**S4**) are the steps taken to perform the error analysis for the zeroth-order approximation. (**S5**)–(**S9**) are the steps for the analysis of the first-order approximation. They are a-posteriori computations, requiring the analytical result (**S1**) and numerical results from (**S2**)–(**S3**). The domain discretization uses standard

Table 4
Error analysis for the zeroth-order approximation for Ex. 1 for which $K_s^\varepsilon(x)$ sequence has circular inclusions, ratio 1000:1; $\widetilde{K}_s^0 = 1.1866 \times 436.60 = 518.09$. Note how the error in the second column is decaying linearly and also that UBE is a reliable error indicator. The gradient and flux sequences are bounded. The grid for $u^0(x)$ was the same as for the fine-scale.

ε	$\|u^\varepsilon - u^0\|_2$	UBE	$\|\nabla u^\varepsilon - \nabla u^0\|_2$	$\|K^\varepsilon \nabla u^\varepsilon - \widetilde{K}^0 \nabla u^0\|_2$	grid ($\sim$)
$(0.5)^1$	2.22e−2	3.65e−2	1.58e−1	3.10e+0	88×88
$(0.5)^2$	1.08e−2	2.17e−2	1.50e−1	2.85e+0	94×94
$(0.5)^3$	4.00e−3	1.21e−2	1.45e−1	2.60e+0	104×104
$(0.5)^4$	3.25e−3	5.92e−3	1.41e−1	2.47e+0	114×114
$(0.5)^5$	1.34e−3	2.31e−3	1.22e−1	2.21e+0	130×130

Table 5
Error analysis for the first-order approximation for Ex. 1. Note how the error in the second column is decaying linearly and it corresponds to about half of the UBE value from Table 4. There was no significant improvement in the error convergence of the gradient.

ε	$\|u^\varepsilon - u_1^\varepsilon\|_2$	UBE	$\|\nabla u^\varepsilon - \widetilde{\mathbf{C}}(y)\nabla u^0\|_2$	$\|K^\varepsilon \nabla u^\varepsilon - \widetilde{K}^0 \widetilde{\mathbf{C}}(y)\nabla u^0\|_2$
$(0.5)^1$	1.34e−2	1.82e−2	2.45e−1	3.47e+0
$(0.5)^2$	8.56e−3	1.08e−2	2.28e−1	3.35e+0
$(0.5)^3$	4.57e−3	6.00e−3	2.28e−1	3.26e+0
$(0.5)^4$	2.89e−3	2.96e−3	2.10e−1	2.96e+0
$(0.5)^5$	1.09e−3	1.15e−3	1.01e−1	2.57e+0

Table 6
Error analysis for the zeroth-order approximation for Ex. 2, where $K_s^\varepsilon(x)$ sequence has square inclusions, ratio 1:100; $\widetilde{K}_s^0 = \mathbf{1.139} \times 1.4901 = 1.6972$. Note how the error in the second column is decaying linearly and also that UBE is a reliable error indicator. The gradient and flux sequences are nearly bounded. Grid for $u^0(x)$ was 40×40 ($\sim$). See also Fig. 6.

ε	$\|u^\varepsilon - u^0\|_2$	UBE	$\|\nabla u^\varepsilon - \nabla u^0\|_2$	$\|K^\varepsilon \nabla u^\varepsilon - \widetilde{K}^0 \nabla u^0\|_2$	grid ($\sim$)
$(0.5)^1$	1.17e−2	1.69e−2	1.02e−1	4.13e−2	130×130
$(0.5)^2$	5.41e−3	8.10e−3	1.08e−1	1.14e−1	130×130
$(0.5)^3$	2.33e−3	4.06e−3	1.12e−1	1.28e−1	130×130
$(0.5)^4$	1.16e−3	1.98e−3	1.13e−1	1.33e−1	130×130
$(0.5)^5$	7.22e−4	9.91e−4	1.14e−1	1.38e−1	281×281

Table 7
Error analysis for the first-order approximation for Ex. 2. Note how the error in the second column is decaying linearly and it corresponds to about half of the UBE value. The error for the gradient and flux sequences improved from Table 6. See also Fig. 7.

ε	$\|u^\varepsilon - u_1^\varepsilon\|_2$	UBE	$\|\nabla u^\varepsilon - \widetilde{\mathbf{C}}(y)\nabla u^0\|_2$	$\|K^\varepsilon \nabla u^\varepsilon - \widetilde{K}^0 \widetilde{\mathbf{C}}(y)\nabla u^0\|_2$
$(0.5)^1$	4.86e−3	8.4e−3	8.09e−2	2.40e−1
$(0.5)^2$	2.61e−3	4.05e−3	6.30e−2	1.91e−1
$(0.5)^3$	1.20e−3	2.03e−3	5.52e−2	1.67e−1
$(0.5)^4$	6.23e−4	9.98e−4	5.40e−2	1.48e−1
$(0.5)^5$	4.48e−4	4.95e−4	5.50e−2	1.45e−1

Table 8
Error analysis for the zeroth-order approximation for Ex. 3. $K_s^\varepsilon(x)$ sequence has square inclusions, and ratio 1e−07:1e−02; $\widetilde{K}_s^0 = \mathbf{1.147} \times 1.51e-07 = 1.73e-07$. The error in the second column is decaying linearly and UBE is a reliable error indicator. The gradient and flux sequences are nearly bounded. Grid size for computing the u^0 was 30×30 ($\sim$). See also Fig. 8.

ε	$\|u^\varepsilon - u^0\|_2$	UBE	$\|\nabla u^\varepsilon - \nabla u^0\|_2$	$\|K^\varepsilon \nabla u^\varepsilon - \widetilde{K}^0 \nabla u^0\|_2$	grid ($\sim$)
$(0.5)^1$	2.87e−1	4.54e−1	2.77e+0	7.00e−10	130×130
$(0.5)^2$	1.96e−1	2.70e−1	3.50e+0	6.97e−10	130×130
$(0.5)^3$	1.19e−1	1.50e−1	4.14e+0	6.79e−10	130×130
$(0.5)^4$	6.74e−2	7.50e−2	4.39e+0	6.39e−10	130×130
$(0.5)^5$	3.65e−2	3.70e−2	4.08e+0	5.60e−10	130×130

Table 9
First-order error analysis for Ex. 3. The error in the second column is decaying linearly and it corresponds to about half of the UBE value from Table 8. The error for the gradient and flux sequences generally improved from Table 8. See also Figs. 9–11.

ε	$\|u^\varepsilon - u_1^\varepsilon\|_2$	UBE	$\|\nabla u^\varepsilon - \widetilde{\mathbf{C}}(y)\nabla u^0\|_2$	$\|K^\varepsilon \nabla u^\varepsilon - \widetilde{K}^0 \widetilde{\mathbf{C}}(y)\nabla u^0\|_2$
$(0.5)^1$	2.65e−1	2.27e−1	3.45e+0	4.35e−12
$(0.5)^2$	1.49e−1	1.35e−1	3.29e+0	4.22e−12
$(0.5)^3$	7.78e−2	7.50e−2	4.60e+0	4.15e−12
$(0.5)^4$	3.95e−2	3.75e−2	3.06e+0	4.01e−12
$(0.5)^5$	2.18e−2	1.85e−2	2.72e+0	3.50e−12

linear conforming finite triangular elements. Mesh refinement was used when solving the fine-scale problems until the error decreased to acceptable values. For example, in the tables, the grid size 130×130 ($\sim$) is an approximation of the number of triangular nodes in each direction. The nonlinear systems were solved by Newton–Raphson iterative scheme. There was no constraint imposed between the matrix and inclusion, other than the standard assumption of the flux continuity across the interface.

By looking at the Tables 4–9, similar convergence patterns are observed for different BVP's, shapes of inclusion, and inclusion ratio. Therefore the summary of the results are discussed towards the end.

4.2.1. Example 1
The BVP describes a flow from the left lower corner of the domain, $\Omega_1 = [0, 0.05]^2$, to the right upper corner $\Omega_2 = [0.95, 1]^2$, with no-flow boundary elsewhere.

$$\begin{cases} \nabla \cdot q^\varepsilon = 0 & x \in \Omega \\ u^\varepsilon(x) = 1.5 & x \in \Omega_1 \\ u^\varepsilon(x) = 1 & x \in \Omega_2 \\ K^\varepsilon(x, u^\varepsilon(x))\frac{\partial u^\varepsilon}{\partial \eta} = 0 & \partial\Omega \setminus \Omega_1 \cup \Omega_2 \end{cases}$$
$$\approx \begin{cases} \nabla \cdot q^0 = 0 & x \in \Omega \\ u^0(x) = 1.5 & x \in \Omega_1 \\ u^0(x) = 1 & x \in \Omega_2 \\ K^0(x, u^0(x))\frac{\partial u^0}{\partial \eta} = 0 & \partial\Omega \setminus \Omega_1 \cup \Omega_2 \end{cases}. \tag{32}$$

The results are presented in Tables 4 and 5 where we have used $K_s^\varepsilon(x)$ with ratio 1000:1 and circular inclusions with conductivity function given by the van Genuchten's relationship:

$$K^\varepsilon(x, u^\varepsilon(x)) = K_s^\varepsilon(x)((1 + |\alpha u^\varepsilon(x)|^n)^{-m})^p [1 - (1 - (1 + |\alpha u^\varepsilon(x)|^n)^{-1})^m)^2, \tag{33}$$

and parameters: $\alpha = 1.04 \text{ m}^{-1}$, $m = 0.283, n = 1 \setminus (1 - m)$ and $p = 0.5$ [29].

4.2.2. Example 2
This example is the classical nonlinear Dirichlet problem. Based on our experience, this is the most challenging of our examples in terms of obtaining good convergence rates.

$$\begin{cases} \nabla \cdot (K^\varepsilon(x, u^\varepsilon(x))\nabla u^\varepsilon(x)) = 1 & x \in \Omega \\ u^\varepsilon(x) = 0 & x \in \partial\Omega \end{cases}$$
$$\approx \begin{cases} \nabla \cdot (K^0(u^0(x))\nabla u^0(x)) = 1 & x \in \Omega \\ u^0(x) = 0 & x \in \partial\Omega \end{cases}. \tag{34}$$

The relative permeability function applied here is known as Gardner's relationship:

$$K^\varepsilon(x, u^\varepsilon(x)) = K_s^\varepsilon(x) \exp(\alpha|u^\varepsilon(x)|) \tag{35}$$

with $\alpha = 3 [\text{m}^{-1}]$ [29] and, $K_s^\varepsilon(x)$ describing square inclusions with ratio 1:100. The analysis of the errors between the approximations are summarized in Tables 6 and 7 and illustrated in Figs. 6 and 7.

4.2.3. Example 3 – Steady-state with gravity forcing - evaporation from a water table
In this example, we apply the results above for low Preclet number condition, meaning the capillary pressure dominates over gravity. In such a case, the effective tensor remains the same as without gravity [6]. When gravity is considered, Darcy's law has the form:

$$q^\varepsilon(x) = -\frac{K_s^\varepsilon(x)k_r(u^\varepsilon(x))}{\mu} \nabla(u^\varepsilon - \rho g \nabla x_2)$$
$$= -K^\varepsilon(u^\varepsilon(x))\nabla(u^\varepsilon - \rho g \nabla x_2), \tag{36}$$

where x_2 is the direction of gravity. This example describes a steady-state flow (evaporation) through an unsaturated vertical profile, (c.f. [29]), from a more saturated region $\Gamma^1 = [x_1, 0]$, where capillary pressure is $u(x) = -2[m]$, to the less saturated region (soil surface), $\Gamma^3 = [x_1, 1]$ with $0 \leqslant x_1 \leqslant 1$ where $u(x) = -6[m]$. There is no-flow boundary on the sides $\Gamma^2 = [0, x_2]$ and $\Gamma^4 = [1, x_2]$ with $0 \leqslant x_2 \leqslant 1$:

$$\begin{cases} \nabla \cdot q^\varepsilon = 0 & x \in \Omega \\ u^\varepsilon(x_1, 1) = -6, u^\varepsilon(x_1, 0) = -2 & x \in \Gamma^1 \cup \Gamma^3 \\ K^\varepsilon \frac{\partial u^\varepsilon}{\partial \eta} = 0 & x \in \Gamma^2 \cup \Gamma^4 \end{cases}$$
$$\approx \begin{cases} \nabla \cdot q^0 = 0 & x \in \Omega \\ u^0(x_1, 1) = -6, u^0(x_1, 0) = -2 & x \in \Gamma^1 \cup \Gamma^3 \\ K^0 \frac{\partial u^0}{\partial \eta} = 0 & x \in \Gamma^2 \cup \Gamma^4 \end{cases} \tag{37}$$

with $\partial\Omega = \bigcup_{i=1}^4 \Gamma^i$. Note that one can consider this BVP as a particular case of (1) with a highly oscillatory forcing $f^\varepsilon(x) =$
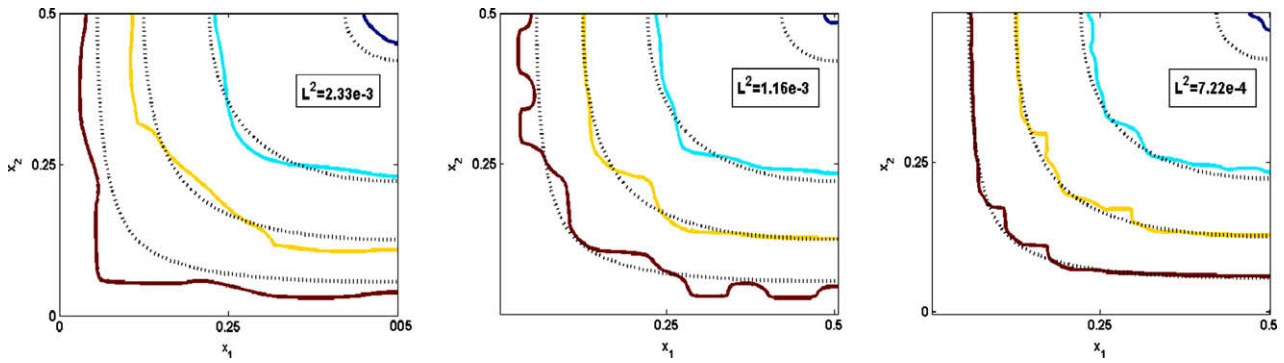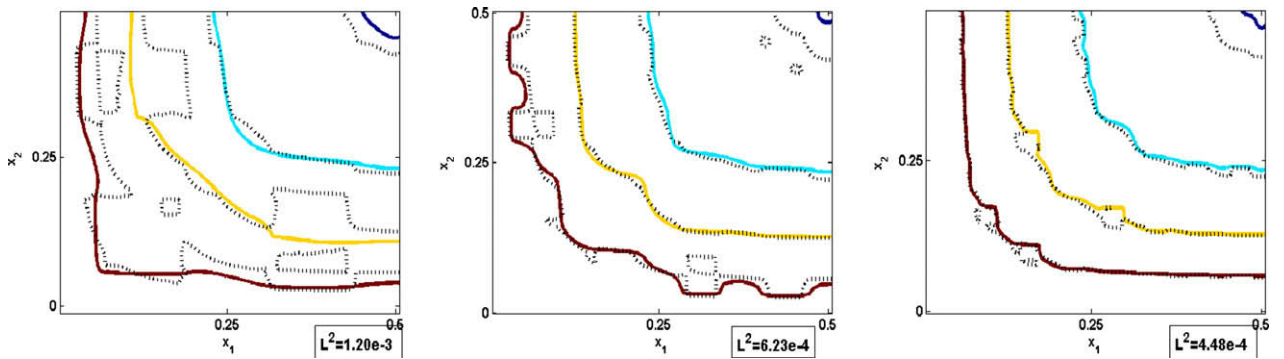
Fig. 6. A quarter of the unit domain showing the fine-scale (solid) and zeroth-order $u^0(x)$, (dashed) for $\varepsilon = (0.5)^3, (0.5)^4, (0.5)^5$, respectively, from Table 6, Example 2. Contours values are from the boundary to the inside $u(x) = -0.01, -0.02, -0.03, -0.04$, respectively. Note that $u^0(x)$ smooths out oscillations from the heterogeneities, in contrast with $u_1^\varepsilon(x)$ for the same problem, illustrated in Fig. 7.

Fig. 7. A quarter of the unit domain showing the fine-scale (solid) and first-order $u_1^\varepsilon(x)$ (dashed) for $\varepsilon = (0.5)^3, (0.5)^4, (0.5)^5$, respectively, from Table 7, Example 2. Contours values are from the boundary to the inside $u(x) = -0.01, -0.02, -0.03, -0.04$, respectively. Note how $u_1^\varepsilon(x)$ captures the heterogeneous features that were averaged out from Fig. 6, and the error dropped to about half of the error obtained by the $u^0(x)$ approximation.
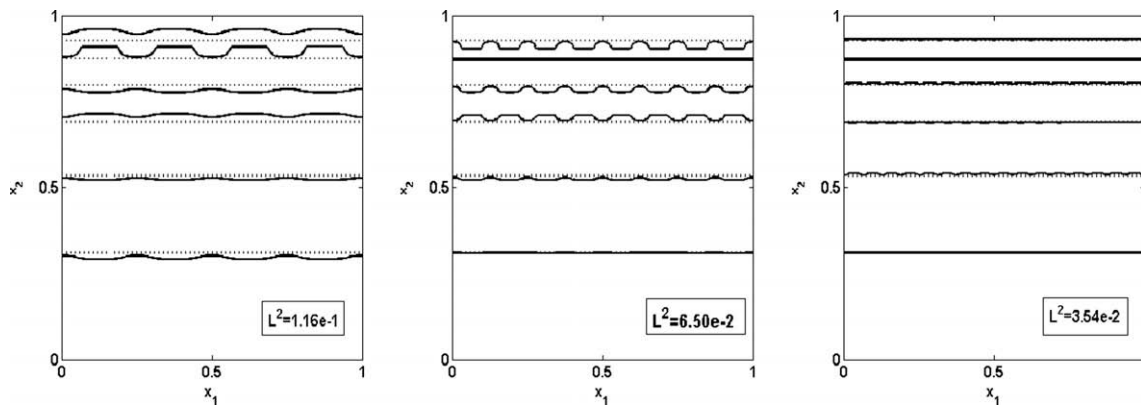

Fig. 8. Fine-Scale (solid) and zeroth-order $u^0(x)$, (dashed) for $\varepsilon = (0.5)^3, (0.5)^4, (0.5)^5$, respectively, from Table 8, Example 3. The contours are from top to bottom $u(x) = -5, -4.5, -4, -3.5, -3, -2$, respectively. Note that $u^0(x)$ smooths out oscillations from the heterogeneities, in contrast with $u_1^\varepsilon(x)$ for the same problem, shown at Fig. 9 ahead.

$\rho g \nabla \cdot (K^\varepsilon(x) \nabla x_2)$. The conductivity function is given by the Brooks and Corey relationship:

$$K^\varepsilon(x, u^\varepsilon(x)) = K_s^\varepsilon(x)(|\alpha u^\varepsilon(x)|)^{-\frac{2m+3}{m}}, \tag{38}$$

where $\alpha = 1.71[\text{m}^{-1}]$ and parameter $m = 2$ [29]. The results are summarized in Tables 8 and 9, and illustrated in Figs. 8–11. We observe that when capillary pressure is not dominant, the upscaled equation may change [19].

4.2.4. Discussion of the numerical results – Tables 4–9

We recall that the convergence results are for the pressure solution. In general, they demonstrate that the proposed analytical approximations have similar convergence rates with respect to the exact fine-scale solution as the classical zeroth and first-order homogenized approximations based on exact solutions of the respective cell problems. For the first-order, they indicate the same convergence pattern as the classical theoretical results (c.f. e.g. [4,17,24]), proven for linear diffusion problems with
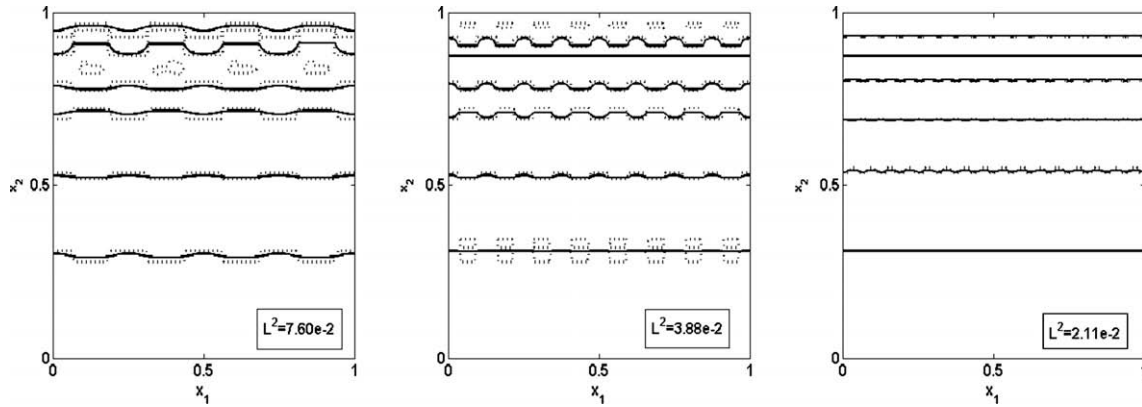
Fig. 9. Fine-Scale (solid) and first-order $u_1^\varepsilon(x)$ (dashed) for $\varepsilon = (0.5)^3, (0.5)^4, (0.5)^5$, respectively, from Table 9, **Example 3**. The contours are from top to bottom $u(x) = -5, -4.5, -4, -3.5, -3, -2$, respectively. Note how $u_1^\varepsilon(x)$ captures the heterogeneous features that were averaged out from Fig. 8, and the error dropped to about half of the error obtained by the $u^0(x)$ approximation.
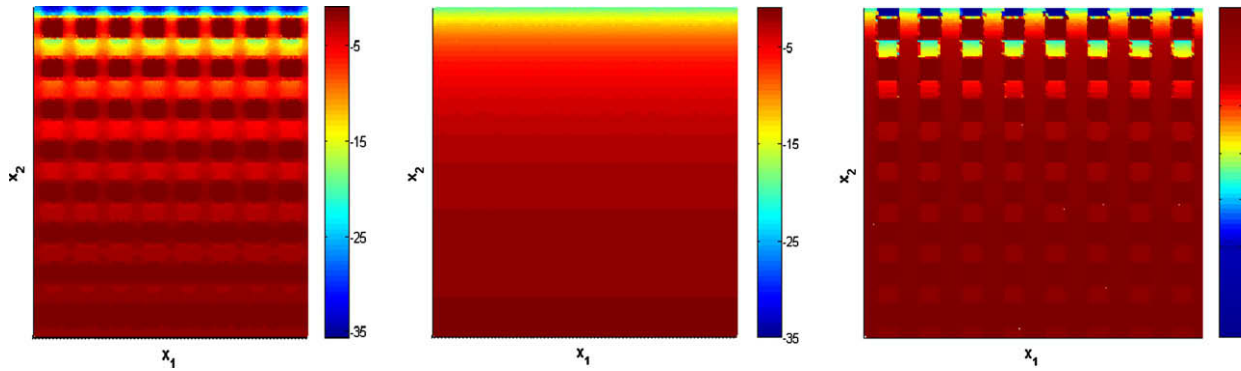

Fig. 10. Comparison between the fine-scale partial derivatives: $\frac{\partial u^\varepsilon}{\partial x_2}$ (left), $\frac{\partial u^0}{\partial x_2}$ (center), and $\widetilde{C}_{22}(y)\frac{\partial u^0}{\partial x_2}$ (right), when $K_s^\varepsilon = (0.5)^4$, from Example 3, Tables 8,9. Note how the right graph is a much better approximation than the one in the center.
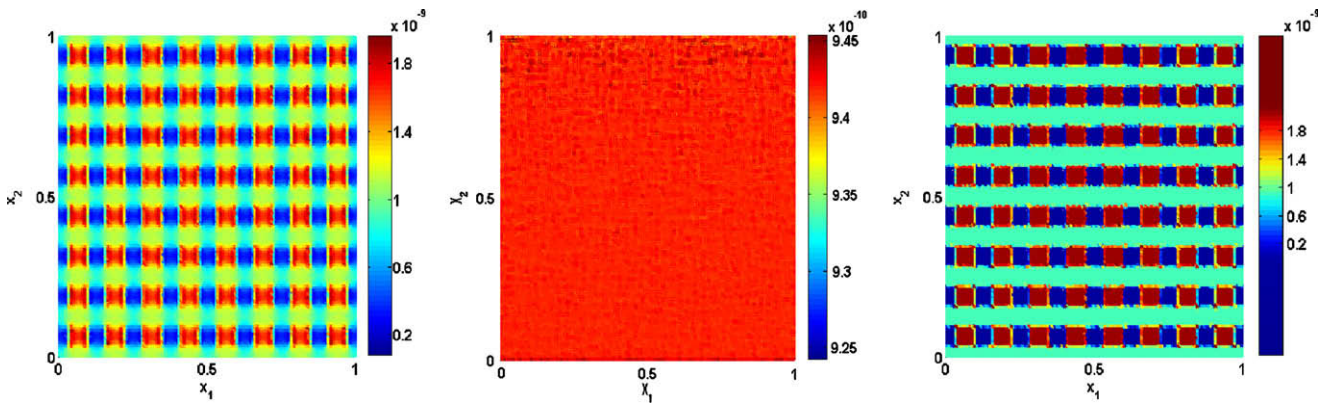

Fig. 11. Comparison between the second component of the fluxes: $K^\varepsilon(x, u^\varepsilon)\nabla u^\varepsilon$ (left), $\widetilde{K}^0(x, u^0)\nabla u^0$ (center) and $\widetilde{K}^0(x, u^0)\widetilde{\mathbf{C}}(\mathbf{y})\nabla u^0$ (right), when $K_s^\varepsilon = (0.5)^4$, from Example 3, Tables 8,9. Note how the upscaled flux on the right incorporates heterogeneous features of the medium, unlike the zeroth-order approximation in the center.

heterogeneous fine-scale coefficient. Further details on each aspect of the convergence is presented next.

(i) The convergence analysis for the zeroth-order approximation agrees with theoretical results, meaning strong convergence in the L^2-norm of the solutions and weak convergence of the gradients and fluxes [6].

(ii) From our experiments, example 2 is the most sensitive to changes in the upscale coefficient, and presented the most difficulty in obtaining good convergence results. We point that out because similar convergence behavior was obtained in the other examples, by using upscaled coefficients within 5% of our analytical value. However, the example 2 did not present similar convergence behavior. Because of its sensitivity of the error to the upscaled approximation, this kind of problem may be considered as a benchmark to various upscaling procedures, and will also be explored in a future study.

(iii) The error indicator (UBE) was accurate for all the cases, demonstrating that the proposed analytical approximation for the basis functions is indeed capturing the error.

(iv) The first-order approximation is also converging strongly in L^2-norm. Moreover, the error indicator (UBE) in the solution dropped to about half of the respective zeroth-order, corresponding to a more accurate approximation. This result occurs despite the small scale structure observed by adding the first-order term, illustrated in Figs. 7 and 9. This variability of the corrector, which has the appearance of a numerical noise, becomes negligible as the scale parameter goes to zero. To make sure that these features did not result from using the approximation $\tilde{w}^i(y) \in L^2(\Omega)$, we performed the same simulations using the numerical solution $w^i(y) \in H^1(\Omega)$, and these small scale features were also observed. This indicates that they are indeed a characteristic of the first-order approximations of these nonlinear cases. We note that they did not appear when applying the results to the linear case [26,27].

(v) Note how the first-order correction provides a significant improvement for the gradient approximation in Table 7 and flux approximation in Table 9, and also illustrated on Figs. 10 and 11. We observe that the absolute value of the error is smaller than the zeroth-order approximation, in general. However, the gradient and flux estimates may be polluted by the small scale features of the first-order approximation, which is likely to also be the cause of the non-monotone behavior of the error sequences.

(vi) In general, we observe that the sequence of gradients and fluxes are at least bounded as stated before on Eqs. (29) and (30), therefore convergence up to a subsequence is expected. Note that boundedness may also be an important property for many applications. An improvement in these errors may be achieved by using, for example, nonconforming finite element or mixed finite element discretization methods.

5. Conclusion

In this paper we proposed an analytical procedure for obtaining the effective coefficient when the medium is composed of centered symmetric inclusions, which allow a zeroth and a first-order approximation to a nonlinear BVP (1). The first-order was possible by using an analytical approximation to the basis functions. To demonstrate that our results provide a valid description of the flow behavior, we performed convergence analysis that corroborates theoretical convergence results from the classical literature. In the same literature, the extension to more general nonlinear problems, including multiphase systems, has also been proved to be possible.

Even though we only apply this analytical computation to media containing block inclusions symmetrically centered in the grid cell, the procedure is general in nature. This particular case allows one to demonstrate that, in such cases, the upscale coefficient is a diagonal tensor and it is a necessary step towards more generalized cases, by considering a given media as a superposition of such geometries, which can further extend to random media, for example. Generalization to non-periodic media is possible and is also an ongoing work. Numerical application of the zeroth-order results to multiphase transient cases is possible [1,2,8]. Another possible venue for further applications includes multilevel solvers and adaptive modeling algorithms.

Appendix

The macroscopic Eq. (6), which is the result of upscaling of equations of type (1), is well known [4,24]; however the details of deriving it by the formal asymptotic expansion method are not easily accessible in the literature. For the benefit of the reader, a detailed derivation of the upscaled Eq. (6) along with the cell problems (10) using the formal asymptotic expansion (5) is given in this appendix.

We consider a nonlinear relationship of type (3), where the spatial variability is periodic and specified by the tensor $K_s^\varepsilon(x)$. Following the classical approach of two-scale asymptotic expansion, we first consider x and y as independent variables. Thus, given a function $\phi_\varepsilon(x) = \phi(x, y)$ and using $y = \frac{x}{\varepsilon}$, we note that differentiation of the function ϕ_ε becomes:

$$\frac{d\phi_\varepsilon}{dx_i} = \frac{\partial \phi}{\partial x_i} + \frac{1}{\varepsilon}\frac{\partial \phi}{\partial y_i}. \tag{39}$$

Consequently, we use the notation $\nabla \to \nabla_x + \varepsilon^{-1}\nabla_y$. Let us also recall the Y-averaging operator:

$$\langle \phi(x, y)\rangle_Y = \frac{1}{|Y|}\int_Y \phi(x, y)dy. \tag{40}$$

Now, consider the following Taylor expansion of the permeability K around the point (y, u^0):

$$\begin{aligned}
K(y, u^\varepsilon) &= K(y, u^0 + \varepsilon(u^1 + \varepsilon u^2 + \ldots)) \\
&= K(y, u^0) + \varepsilon(u^1 + \varepsilon u^2 + \ldots)\frac{\partial K}{\partial u}(y, u^0) + \mathcal{O}(\varepsilon^2) \\
&= K(y, u^0) + \varepsilon u^1 \frac{\partial K}{\partial u}(y, u^0) + \mathcal{O}(\varepsilon^2).
\end{aligned} \tag{41}$$

In the following we shall assume that $\frac{\partial K}{\partial u}$ is of order $\mathcal{O}(1)$ or higher. Our goal is to substitute the expansions (5) and (41) into the fine-scale Eq. (1) and collect the powers of ε.

First, by combining (5) with (39) one obtains

$$\nabla u^\varepsilon = \varepsilon^{-1}\nabla_y u^0 + \varepsilon^0(\nabla_x u^0 + \nabla_y u^1) + \varepsilon^1(\nabla_x u^1 + \nabla_y u^2) + \cdots$$

Substituting the last equation into (1) and applying again (39) to the divergence operator one obtains:

$$\begin{aligned}
-f(x) = \nabla \cdot (K(y, u^\varepsilon)\nabla u^\varepsilon) &= \varepsilon^{-2}[\nabla_y \cdot (K(y, u^\varepsilon)\nabla_y u^0)] \\
&+ \varepsilon^{-1}[\nabla_x \cdot (K(y, u^\varepsilon)\nabla_y u^0) + \nabla_y \cdot (K(y, u^\varepsilon)(\nabla_x u^0 + \nabla_y u^1))] \\
&+ \varepsilon^0[\nabla_x \cdot (K(y, u^\varepsilon)(\nabla_x u^0 + \nabla_y u^1)) \\
&+ \nabla_y \cdot (K(y, u^\varepsilon)(\nabla_x u^1 + \nabla_y u^2))] + \mathcal{O}(\varepsilon).
\end{aligned} \tag{42}$$

Next, the Taylor expansion (41) is substituted into the last equation. Considering the fact that (41) starts at order ε^0, one immediately observes that at order ε^{-2} in Eq. (42) one gets:

$$\nabla_y \cdot (K(y, u^0)\nabla_y u^0) = 0$$

This is a differential equation for the Y-periodic function $u^0(\cdot, y)$ with zero right-hand side. Hence, the solution is constant in y, that is:

$$u^0(x, y) = u^0(x).$$

In particular this also implies that $\nabla_y u^0 \equiv 0$, and as a consequence the first term in the third line of Eq. (42) becomes identically zero. Therefore, we can now collect powers of ε^{-1} in Eq. (42). These will come only from the remaining term in the third line, which, with the help of (41) yields:

$$\nabla_y \cdot (K(y, u^0)(\nabla_x u^0 + \nabla_y u^1)) = 0.$$

Observe now, that this is a linear differential equation for the Y-periodic function $u^1(\cdot, y)$. Its general solution can be expressed in the form:

$$u^1(x,y) = c + \sum_{i=1}^{d} w^i(y,u^0)\frac{\partial u^0}{\partial x_i}x. \qquad (43)$$

where w^i, $i = 1, \ldots, d$ are the solutions to the d cell problems

$$\nabla_y \cdot (K(y,u^0)\nabla_y w^i) = -\nabla_y \cdot (K(y,u^0)e_i) \qquad (44)$$

and c (may even be a function of x) is independent of y and accounts for the boundary of $u^1(x,y)$. Due to the special form (3) of the conductivity, the last equation reduces to Eq. (10). Note also, that we obtain the same type of cell problems as in the case of linear diffusion equation with oscillatory coefficients, c.f. e.g. [7].

Finally, we collect terms at order ε^0 in Eq. (42). These will come from the second term in the third line and the two terms in the fourth line. We obtain:

$$\nabla_y \cdot \left(u^1 \frac{\partial K}{\partial u}(y,u^0)(\nabla_x u^0 + \nabla_y u^1) + K(y,u^0)\nabla_x u^1 + \nabla_y u^2 \right)$$
$$+ \nabla_x \cdot (K(y,u^0)(\nabla_x u^0 + \nabla_y u^1)) + f(x)$$
$$= 0. \qquad (45)$$

Now, $u^1(\cdot, y)$ and $u^2(\cdot, y)$ are Y-periodic functions, and thanks to its special form (Eq. (3)), so is $\frac{\partial K}{\partial u}(y,u^0)$. As a result we can apply the Y-averaging operator (40) to the last Eq. (45), and, using the divergence theorem and periodicity, obtain:

$$-\frac{1}{|Y|}\int_Y \nabla_x \cdot (K(y,u^0)(\nabla_x u^0 + \nabla_y u^1))dy = f(x). \qquad (46)$$

The last equation, with the help of Eq. (43), can be written as:

$$-\nabla_x \cdot (K^0(u^0(x))\nabla_x u^0) = f(x).$$

Here, the homogenized permeability tensor K^0 is given by:

$$K^0(u^0(x)) = \frac{1}{|Y|}\int_Y K(y,u^0(x))[\mathbf{I} + \nabla_y \mathbf{w}(y)^t]dy, \qquad (47)$$

where $\mathbf{I}$ is the identity tensor and $\mathbf{w}$ is the vector of the cell solutions (44), that is, $\mathbf{w} = (w^1, \ldots, w^d)$. In component form, the last equation reads:

$$K^0_{ij}(u^0(x)) = \frac{1}{|Y|}\int_Y \left[K_{ij}(y,u^0(x)) + \sum_{l=1}^{n} K_{il}(y,u^0(x))\frac{\partial w^j}{\partial y_l}(y) \right] dy. \qquad (48)$$

Observe that the above derivation can easily be extended to $K_s = K_s(x, x/\varepsilon)$, the non-uniform oscillating function, that is with slow dependence of K_s on x at the coarse scale.

References

[1] B. Amaziane, A. Bourgeat, J. Koebbe, Numerical simulation and homogenization of two-phase flow in heterogeneous porous media, Trans. Porous Media 6 (1991) 519–547.

[2] B. Amaziane, T. Hontans, J.V. Koebbe, Equivalent permeability and simulation of two-phase flow in heterogeneous porous media, Comp. Geosci. 5 (2001) 279–300.

[3] T. Arbogast, Analysis of a two-scale, locally conservative subgrid upscaling for elliptic problems, SIAM J. Num. Anal. 42 (2) (2004) 576–598.

[4] A. Bensoussan, J.L. Lions, G. Papanicolau, Asymptotic Analysis for Periodic Structures, North-Holland, 1978.

[5] J.F. Bourgat, Numerical experiments of the homogenization method for operators with periodic coefficient, in: R. Glowinski, J.L. Lions (Eds.), Computing Methods in Applied Science and Engineering, I, Versailles, December 5–9, 1977, Springer-Verlag, 1978, p. 330.

[6] A. Bourgeat, Two-phase flow, in: U. Hornung (Ed.), Homogenization and Porous Media, Interdisciplinary Applied Mathematics, vol. 6, Springer-Verlag, 1997.

[7] D. Cioranescu, P. Donato, An introduction to homogenization, Oxford Lect. Ser. Math. Appl. 17 (1999).

[8] L.J. Durlofsky, Numerical calculation of equivalent grid block permeability tensors for heterogeneous media, WRR 27 (1991) 699–708.

[9] L.J. Durlofsky, R.C. Jones, W.J. Miliken, A nonuniform coarsening approach for the scale-up of displacement processes in heterogeneous porous media, Adv. Water Resour. 20 (1997) 335–347.

[10] Y. Efendiev, T. Hou, V. Ginting, Multiscale finite element methods for nonlinear partial differential equations, Commun. Math. Sci. 2 (4) (2004).

[11] Y. Efendiev, L. Durlofsky, Accurate subgrid models for two phase flow in heterogeneous reservoirs, SPE J. 9 (2004) 219–226.

[12] Y. Efendiev, L. Durlofsky, Numerical modeling of subgrid heterogeneity in two phase flow simulations, Water Resour. Res. 38 (8) (2002) 1128.

[13] Y. Efendiev, T. Hou, V. Ginting, R. Ewing, Accurate multiscale finite element methods for two-phase flow simulations, JCP 220 (2006) 155–174.

[14] U. Hornung (Ed.), Homogenization and Porous Media, Interdisciplinary Appl. Math., vol. 6, Springer-Verlag, 1997.

[15] T.Y. Hou, X.H. Wu, A multiscale finite element method for elliptic problems in composite materials and porous media, J. Comp. Phys. 134 (1997) 169–189.

[16] T.J.R. Hughes, G.R. Feijó, L. Mazzei, J.B. Quincy, The variational multiscale method – a paradigm for computational mechanics, Comp. Meth. Appl. Mech. Engrg. 166 (1998) 3–24.

[17] V.V. Jikov, S.M. Kozlov, O.A. Oleinik, Homogenization of Differential Operators and Integral Functionals, Springer-Verlag, 1994.

[18] J.B. Keller, Effective conductivity of periodic composites composed of two very unequal conductors, J. Math. Phys. 28 (10) (1987).

[19] J. Lewandowska, J.P. Laurent, Homogenization modeling and parametric study of moisture transfer in an unsaturated heterogeneous porous medium, Trans. Porous Media 45 (2001) 321–345.

[20] J.T. Oden, S. Prudhomme, A. Romkes, P. Bauman, Multi-scale modeling of physical phenomena: adaptive control of models, SIAM J. Sci. Comp. 28 (6) (2006) 2359–2389.

[21] J.D. Moulton, J.E. Dendy, J.M. Hyman, The black box multigrid numerical homogenization algorithm, J. Comp. Phys. 142 (1998) 80–108.

[22] M. Peszynska, M.F. Wheeler, I. Yotov, Mortar upscaling for multiphase flow in porous media, Comput. Geosci. 6 (2002) 73–100.

[23] Ph. Renard, G. De Marsily, Calculating equivalent permeability: a review, Adv. Water Resour. 20 (5-6) (1997) 253–278.

[24] E. Sanchez-Palencia, Non Homogeneous Media and Vibration Theory, Lectures Notes in Physics, 127, Springer-Verlag, Berlin, 1980.

[25] R.F. Sviercoski, C.L. Winter, A.W. Warrick, Analytical approximation for the generalized Laplace's equation with step function coefficient, SIAM J. Appl. Math. 68 (5) (2008) 1268–1281.

[26] R.F. Sviercoski, B.J. Travis, J.M. Hyman, Analytical effective coefficient and first-order approximation for linear flow through block permeability inclusions, Comp. Math. Appl. 55 (2008) 2118–2133.

[27] R.F. Sviercoski, B.J. Travis, Analytical effective coefficient and first-order approximation to linear Darcy's law through block inclusions, in: I. Lirkov, S. Margenov, J. Waśniewski (Eds.), Lecture Notes in Computer Sciences, vol. 4818, Springer, 2008, pp. 267-274.

[28] L. Tartar, Quelques Remarques sur L'homogeneisation, in: H. Fujita (Ed.), Functional Analysis and Numerical Analysis Proceedings Japan–France Seminar, Japanese Society for the Promotion of Science (1976) 468–482.

[29] A.W. Warrick, Soil Water Dynamics, Oxford, 2002.

[30] J. Xu, Two-grid discretization techniques for linear and nonlinear PDEs, SIAM J. Num. Anal. 33 (1996) 1759–1777.